Available online at www.sciencedirect.com
ScienceDirect
International Journal of Thermal Sciences 47 (2008) 749–757
International Journal of Thermal Sciences
www.elsevier.com/locate/ijts

Application of pressure and temperature sensitive paints for study of heat transfer to a circular impinging air jet

Quan Liu, A.K. Sleiti *, J.S. Kapat

Mechanical, Materials and Aerospace Engineering Department, University of Central Florida, Orlando, FL 32816, USA

Received 30 January 2007; received in revised form 25 April 2007; accepted 13 June 2007

Available online 1 August 2007

Abstract

Experimental and computational studies are performed to study pressure and temperature distributions and flow patterns on impingement target surface subject to a single impinging air jet from a plenum. The experiments cover a range of jet-to-target plate distance, Z/D, from 1.5 to 12 for Reynolds number range from 10 000 to 60 000. The main objective is to investigate the optimal jet-to-target distance (Z/D) for stagnation point heat transfer and location of second peak in local heat transfer at small Z/D value under the current jet impingement configuration. Pressure and temperature sensitive paints measurements techniques are implemented to obtain the distribution of pressure and temperature on target surface. The optimal separation distance (Z/D) for stagnation region *Nu* is found to be about 5. The location of the second peak in local *Nu* for Z/D of 1.5 is at radial location (r/D) of about 1.8. The area averaged Nusselt numbers are compared to those calculated using correlation from open literature. The agreement varies with Z/D and jet Reynolds number. Experimental results are also compared to computational (CFD) prediction using realizable k–ε turbulence model.

Keywords: Pressure sensitive paints; Temperature sensitive paints; Impinging air jet; Optimal jet-to-target distance; Second peak

1. Introduction

Jet impingement cooling and heating techniques have attracted many investigators because of their eminent potential to increase local heat and mass transfer. In gas turbine industry, impingement cooling finds use in the cooling of gas turbine parts including blades, vanes, endwalls and disks.

There have been numerous experimental and numerical investigations on flow and heat transfer characteristics of impinging jets. Goldstein and Behbahani [1] investigated the radial distribution of the recovery factor and the local, as well as averaged heat transfer for an axisymmetric impinging air jet formed by a smooth nozzle. Goldstein and Timmers [2] measured the heat transfer coefficient distribution of a single and an array of jets, using liquid crystal visualization technique. Sparrow and Goldstein [3] studied effect of nozzle-to-surface separation distance on local heat transfer for a jet in a crossflow. Martin [4], Han et al. [5], Downs and James [6], Viskanta [7] have given comprehensive reviews on jet impingement heat transfer. Consider the jet nozzles that have been used, there are two extreme types: (i) tube type nozzle, which has large length to diameter ratio (L/D). At the nozzle exit, the initial velocity profile is similar to that of pipe flow. (ii) Orifice in a wall type of nozzle, which has ratio of L/D close to unity. Most nozzles used in literature fall between these two extremes, according to Livingood and Hrycak [8]. The second type of jet nozzle is more similar to those employed in jet impingement design in gas turbine components and is considered in this study. The target surface of impingement within turbine components, typically turbine endwalls, midchord regions of turbine vanes and blades, can be approximated as flat surfaces.

Gardon and Cobonpue [9] measured local heat transfer coefficient for both single and multiple round turbulent jets with Reynolds number varied from 7000 to 112 000 and range of Z/D studied was 1.5 to 15. They reported large variation of stagnation point heat transfer between $Z/D = 1.5$ and $Z/D = 15$. The maximum stagnation point heat transfer was found to occur at $6 < Z/D < 7$. Other researchers also reported the ex-

* Corresponding author.
E-mail address: asleiti@mail.ucf.edu (A.K. Sleiti).

1290-0729/$ – see front matter
doi:10.1016/j.ijthermalsci.2007.06.018

Nomenclature

Amp	amperage of the power input
D	jet nozzle diameter
h	heat transfer coefficient
I	luminescent intensity
I_{ref}	intensity of luminescence under the reference condition
I_R	intensity ratio
k_{air}	thermal conductivity of air
k_f	thermal conductivity of Inconel foil
L	length of jet nozzle
Nu	Nusselt number, hD/k
Nu_o	Nusselt number at stagnation point
Nu_{avg}	area-averaged Nu
P	static pressure
P_o	static pressure at stagnation point
Pr	Prandtl number, $c_p\mu/k$
P_{ref}	pressure under a reference condition
PSP	pressure sensitive paint
q''_{cond}	conduction heat loss
q''_e	effective heat flux of the foil
q'''_{gen}	volume heat generation
q''_{rad}	radiation heat loss
r	distance along plate from stagnation point
Re	jet Reynolds number, U_eD/υ
T_j	total temperature of jet
T_R	reference temperature
TSP	temperature sensitive paint
T_w	wall temperature
U	velocity in axial direction
U_m	centerline jet velocity
U_e	average velocity at nozzle ext
u'	R.M.S. value of fluctuating component of velocity
V	volume of the heating foil
$Volt$	voltage of the power input
Z	separation distance between jet nozzle and target plate
υ	kinematic viscosity
ρ	density

istence of an optimal separation distance (Z/D) between jet nozzle and the target flat plate (Sparrow et al. [3], Goldstein et al. [10], Gardon and Akfirat [11]). A literature survey by Livingood and Hrycak [8], concluded that the maximum heat transfer coefficient should occur when the impingement plate is separated from the nozzle exit by the length of the potential core. They also pointed out that various core lengths have been obtained by different investigators. Donaldson et al. [12] explained this optimal Z/D by the variation in the stagnation point velocity gradient as a result of the elimination of the potential core and formation of a developed jet. Gardon and Akfirat's [11] explanation can be briefed as follows. At small separation distance the jet velocity within the potential core remains the same. Meanwhile, the turbulence level within the core increases. As a result, stagnation point heat transfer increases. With further increase in separation distance as Z/D beyond the length of potential core, the impinging velocity attenuates and turbulence also decreases, which results in a decrease in stagnation point heat transfer coefficient. A secondary peak away from the stagnation point were observed in local heat transfer coefficient for $Z/D < 6$. There has been considerable disagreement among investigators as to the physical explanation for the second peak in the local heat transfer coefficient. With smoke-wire visualization technique, for small Z/D, Popiel and Trass [13] observed ring-shaped wall eddies induced consecutively by the large-scale toroidal vortices hitting the plate. The wall eddies could be responsible for the enhancement of local heat and mass transfer and possibly for the second peak in local heat transfer coefficient. Gardon and Akfirat [11] explained the second peak in h as the result of transition from laminar to turbulent boundary layers. The transition occurs immediately after the disappearance of flow acceleration, which serves to stabilize the laminar boundary layer in the stagnation zone. Recently Narayanan et al. [14] performed an experimental study of flow field, surface pressure, and heat transfer rates of a submerged, turbulent, slot jet impinging normally on a flat plate with Z/D of 3.5 and 0.5. It was observed that locations of secondary peak in heat transfer correspond to near-wall streamwise fluctuating velocity variance. San and Shiao [15] studied the effects of jet plate size and plate spacing on the heat transfer characteristics for a confined circular air jet vertically impinging on a flat plate. Jet Reynolds number was in the range of 10 000–30 000 and plate spacing-to-jet diameter ratio was between 1 and 6. The authors claimed that the impingement-plate heating condition and flow arrangement of the jet after impingement are two important factors affecting the dependence of the stagnation Nusselt number on Z/D.

In the present work, local heat transfer from a heated target plate to a turbulent round isothermal air jet is measured for various Z/D and jet Reynolds number. The main objective is to investigate the optimal Z/D for stagnation point heat transfer and location of second peak of local heat transfer at small Z/D cases. Temperature sensitive paint (TSP) is applied to measure the impinging surface temperature distribution under steady state operation. The impinging surface static pressure distribution is measured with pressure sensitive paint (PSP) to help understand the flow structure at the impinging surface around the stagnation zone. Free jet centerline velocity and turbulence level are measured with Pitot probe and hot wire anemometer by traversing the probe along a lead screw setup in order to find out the length of the jet potential core as well as the centerline distribution of turbulence intensity. Experimental results are compared to computational (CFD) prediction using realizable k–ε turbulence model. FLUENT CFD commercial package is used for this simulation. The data obtained with the

present jet configuration will be useful to jet impingement design in gas turbine components.

Measurement technique of PSP and TSP

A pressure sensitive paint (PSP) contains luminophores (basically, dye molecules), that luminance in a suitable wavelength range in response to photo-excitation in a shorter wavelength range. Through two radiationless deactivation processes known as thermal- and oxygen-quenching, the luminescent intensity of the paint emission is inversely proportional to local temperature and pressure. Both TSP and PSP incorporate luminescent molecules in paint together with a transparent polymer binder. For TSP, polymer binders are not oxygen permeable and hence TSP is temperature sensitive only. The basic equation for calibrating a PSP image is the following:

$$\frac{I_{\text{ref}}}{I} = A(T) + B(T)\frac{P}{P_{\text{ref}}} \tag{1}$$

where P is the unknown pressure to be measured under the test condition (e.g., in the presence of wind), P_{ref} is the pressure under a reference condition (e.g., in the absence of wind), I_{ref} is the intensity of luminescence under the reference condition, and I is the intensity of luminescence under the test condition. The need for temperature correction arises because A and B depend on temperature.

Fig. 1 shows the schematic of typical experimental setup of PSP/TSP test. Luminescence intensities are sampled over the area of interest using a charge-coupled-device (CCD) camera. The output of the array can be visually represented as an image, with the luminescence intensity displayed in gray scale or pseudo-color.

The ratio of emission intensity of TSP at any temperature T to the emission intensity at a specified reference temperature T_R is

$$I_R = \frac{I(T)}{I(T_R)} = f_n(T; T_R) \tag{2}$$

The function $f_n(T; T_R)$ can be determined by fitting calibration data with a polynomial and this calibration correlation is then

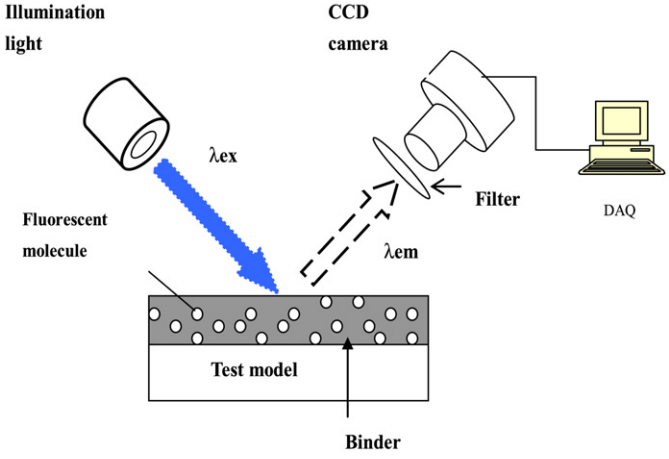

Fig. 1. Schematic of a typical TSP/PSP measurement system.

ready to be used in any TSP experiment. During the experiment, first a wind-off (reference) image is taken to acquire $I(T_R)$ before start the test. The reference temperature is measured at the painted surface. After achieving steady state, a wind-on image is taken to acquire $I(T)$. Then intensity ratio I_R at each pixel location of the picture can be obtained, which is a function of temperature (T) to be measured and the reference temperature (T_R).

A pressure sensitive paint with low temperature sensitivity is applied in the experiment of this paper. It is named Uni-FIB and supplied by ISSI (Innovative Scientific Solution, Inc.). For this certain FIB PSP, the constants A and B in Eq. (1) are not function of temperature under a small range of temperature variation. Since it is a study of isothermal gas jet, a single PSP calibration correlation obtained under the temperature of experimental condition can be applied to the pressure measurement in the test. Similar to TSP, the pressure information at each pixel location can be converted from intensity ratio using the a-prior calibration correlation.

The measurement uncertainties of PSP and TSP are 830 Pascal and 0.9 °C respectively.

Test apparatus

The test unit as shown in Fig. 2 consists of an air supply line, a diffuser, a plenum and a setting chamber. Jet air is introduced into the plenum chamber from a compressor–tank system, which is designed for a blow-down type supersonic wind tunnel. A pressure regulator is installed in the air supply line to control the flow rate in addition to a shutoff valve. A McMillan thermal mass gas flow meter is installed at the inlet of the diffuser to determine the actual flow rate through the jet nozzle. The temperature of air in the chamber is within 1 °C of the ambient temperature for all the tests performed. A 9.5 mm thick Plexiglas plate is attached to the right side of the chamber with a straight hole drilled at the center as the jet nozzle. The diameter of the jet nozzle is also 9.5 mm. The target plate is made of a 12.7 mm thick Plexiglas. To measure the surface pressure distribution, the jet-impinged surface of the Plexiglas plate is painted with PSP coating. The CCD camera sees through the Plexiglas and captures the PSP image from the back side of the target plate. In heat transfer experiments, a 10 cm by 16 cm Inconel foil heater is attached to the impinging side of target plate with two copper bus bars. The thickness of the Inconel foil is 0.5 mm. One side of the Inconel foil is painted with TSP before the foil is attached to the Plexiglas plate. The unpainted side of the foil is facing the jet and the CCD camera again captures the TSP image from the back side of the plate. The temperature difference across the foil is less than 0.05 °C. The separation distance Z/D between the nozzle plate and the target plate are 1.5, 5, 8 and 12. The jet Reynolds numbers that have been tested are 10 000, 20 000, 40 000 and 60 000.

Experimental data reduction

Due to the thickness of the Inconel foil, the constant heat flux assumption is not valid. Instead it is treated as constant

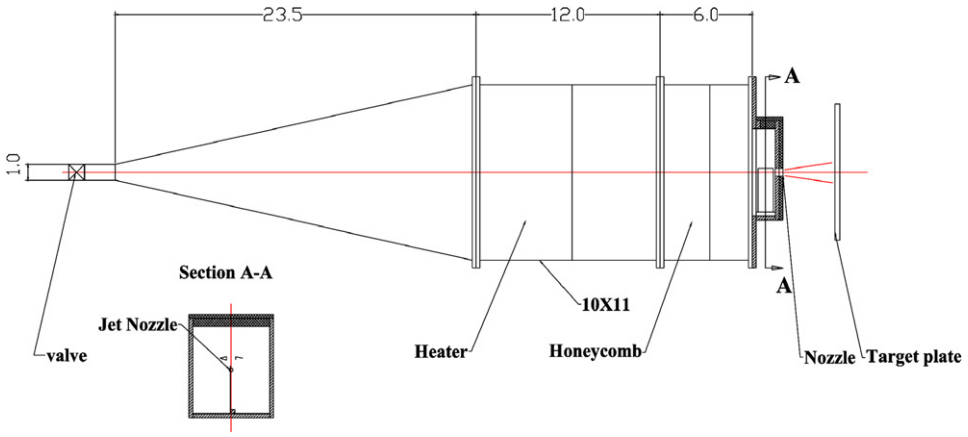

Fig. 2. Schematic of jet impingement rig (unit in inch).

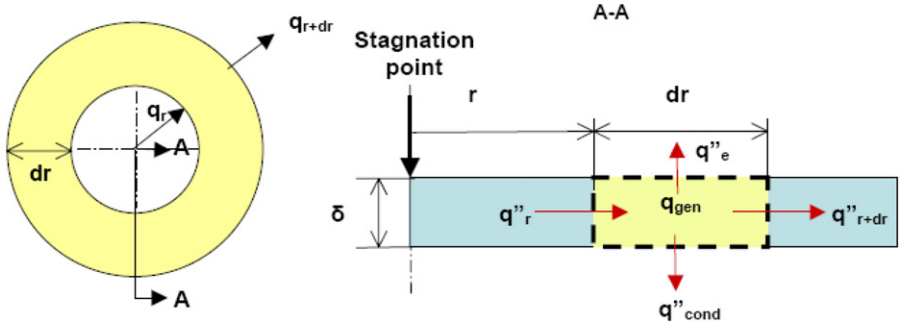

Fig. 3. Differential control volume: $2\pi r\,\mathrm{d}r\delta$, for heat balance analysis in sheet foil (in cylindrical coordinates). Left: cross-section of differential control volume; Right: top view of control volume.

heat generation per unit volume:

$$q'''_{\text{gen}} = \frac{Volt \times Amp}{V} \tag{3}$$

where $q'''_{\text{gen}}(W/m^3)$ is the volume heat generation inside the foil. *Volt* and *Amp* are the voltage and amperage of the power input across the bus bars. V is the volume of the heating foil, which is the heated foil area multiplied by the foil thickness δ.

After obtaining the surface temperature with TSP, the temperature is averaged in circumferential direction due to the axisymmetric pattern of temperature distribution. Then this averaged temperature is plotted as a function of radial distance r (Fig. 12). By applying energy balance to the differential control volume in the foil sheet as shown in Fig. 3, the following form of heat equation is obtained in cylindrical coordinates:

$$q''_r - q''_{r+\mathrm{dr}} - q''_{\text{cond}} + q''_g - q''_e = 0 \tag{4}$$

where

$$q''_r = -k_f \frac{\partial T}{\partial r}, \qquad q''_r - q''_{r+\mathrm{dr}} = \frac{1}{r}\frac{\partial}{\partial r}\left(k_f r \frac{\partial T}{\partial r}\right) \tag{5}$$

q''_e is the effective local surface heat flux that is removed by convection of impinging jet. q''_g is the heat generation term which equals to $q'''_{\text{gen}*}\delta$. q''_{cond} is the conduction heat loss through the Plexiglas plate. The lateral heat conduction term q''_r is induced by the temperature gradient in r direction along the jet impinged foil surface. If the foil were thin enough, the lateral conduction would be negligibly small compared to the heat generation term. k_f is the thermal conductivity of the Inconel foil material. Hence q''_e can be expressed as:

$$q''_e(r) = \frac{1}{r}\frac{\partial}{\partial r}\left(k_f r \frac{\partial T}{\partial r}\right) - q''_{\text{cond}} + q''_g \tag{6}$$

The local heat transfer coefficient h, which is a function of r, can be expressed as:

$$h(r) = \frac{q''_e(r)}{T_w(r) - T_j} = \frac{\frac{1}{r}\frac{\partial}{\partial r}(k_f r \frac{\partial T}{\partial r}) + q''_g - q''_{\text{cond}}}{T_w(r) - T_j} \tag{7}$$

The radiation loss is found to be less than 0.3% of q''_e and is neglected in the heat equation. T_w is the foil surface temperature measured by TSP, and T_j is the total temperature of jet.

Experimental results for heat transfer are presented in terms of Nusselt number:

$$Nu(r) = \frac{h(r)D}{k_{\text{air}}} \tag{8}$$

As the jet is axisymmetric, the radial distribution of Nu can be averaged to give the mean Nusselt number:

$$\overline{Nu} = \frac{2}{R^2}\int_0^R Nu(r) r\,\mathrm{d}r \tag{9}$$

The error in temperature measurement is 0.9 °C. The lowest value of $(T_w - T_j)$ is 15 °C, which corresponds to the maximum uncertainty in h calculation. The uncertainty of q'''_{gen} is 3%.

Therefore, according to the root-sum-square method, the maximum uncertainty in calculating *Nu* is 8.6%.

CFD model

The CFD comparison is performed using FLUENT commercial code. The model consists of $3'' \times 3''$ target plate and $3/8''$ impingement jet of $3/4''$ length (the thickness of Plexiglas nozzle plate) as shown in Fig. 4. The impingement jet is located above the center of the target plate ($3'' \times 3''$ Inconel foil maintained on top of Plexiglas). The four exits are $3''$ width by $0.5625''$ height ($Z/D = 1.5$). The bottom wall is 0.5 mm thick Inconel foil with constant heat flux. The jet is issuing into the target plate in the $-Z$ direction and exits in the X and Y directions. The numerical grid consists of Hex/Wedge grid elements with Cooper grid type. Enhanced near wall treatment option is used to resolve the near wall viscous region with 12 grid points placed in the boundary layer near all walls. For enhanced near wall treatment option, y^+ for the first cell next to a wall is taken less than one. The convergence criterion of the scaled residual for continuity, all three velocity components and turbulent kinetic energy and dissipation rate is set to 10E–6, while for energy equation it is set to 10E–8. The grid is refined until the maximum change in local *Nu* for all cases tested is less than 0.5%. The final mesh consists of 752 000 mesh volumes.

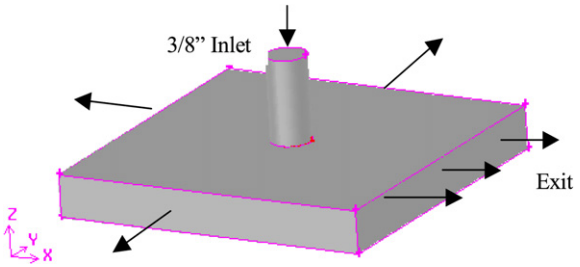

Fig. 4. Geometry and CFD flow domain for single jet.

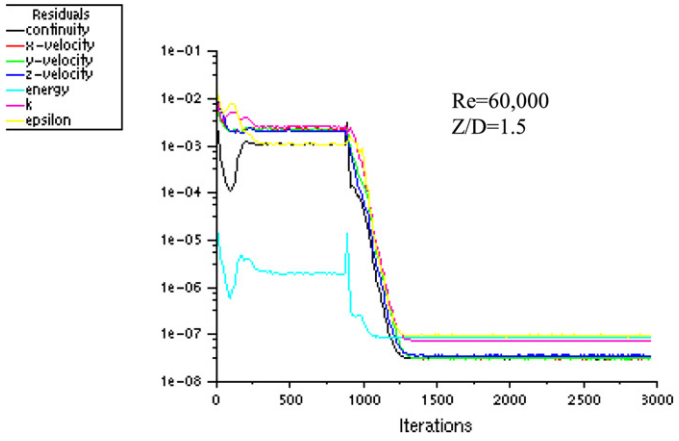

Fig. 5. Scaled residuals: typical convergence history.

At the inlet constant mass flow rate is applied and at all four exits pressure outlet boundary condition is used. Realizable k–ε turbulence model is used for this simulation. The fluid is air with density calculated as for incompressible-ideal gas. Specific heat, conductivity and viscosity are calculated using piecewise linear functions of temperature. SIMPLE algorithm is used for pressure–velocity coupling and second order upwind discretization schemes are used for momentum, TKE, TDR and energy. Fig. 5 shows a typical convergence history in terms of scaled residuals.

Experimental results

The left plot of Fig. 6 shows the free jet centerline velocity distribution measured with Pitot probe. It is found that the length of the potential core is about 4 times the diameter of jet nozzle for $Re = 20\,000$, 40 000 and 60 000. Free jet centerline turbulence distribution is measured with hot wire anemometer. The right plot of Fig. 6 shows the distribution of absolute magnitude of the velocity fluctuations, as shown by the curve of u'/U_m, in which the R.M.S. fluctuation of the centerline velocity (u'), normalized by the local time average centerline velocity (U_m), increases continuously with jet length up to $Z/D = 9$.

Fig. 7 plots the static pressure (in gauge) distribution over the impingement surface measured with PSP for jet Reynolds number of 60 000 and various separation distance Z/D. The region of impingement is marked by the end of negative pressure gradients on the impacted surface. Beyond the impingement region, the pressure is atmospheric.

Concentric contours of isotherms measured by TSP over the impingement surface are shown in Fig. 8 for $Z/D = 1.5$ and 5 with Reynolds number of 10 000 and 60 000. In order to ver-

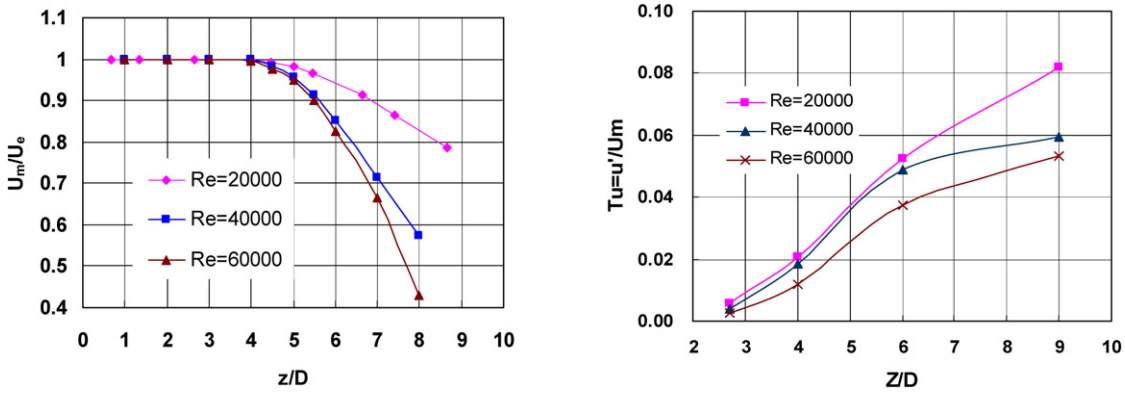

Fig. 6. Distribution of velocity (left) and turbulence intensity (right) on the axis of free jet.

ify the concentric pattern of the temperature distribution, Fig. 9 shows the temperature distribution in circumferential direction at various radius locations. The average temperature fluctuation at each r location is only about 2 to 3 °C, which proves the axisymmetric jet flow condition and, meanwhile, justifies the data reduction procedure. Fig. 10 shows the typical circumferentially averaged temperature distribution as a function of radial distance r. The temperature distribution of each test run is curve-fitted into high-order polynomial.

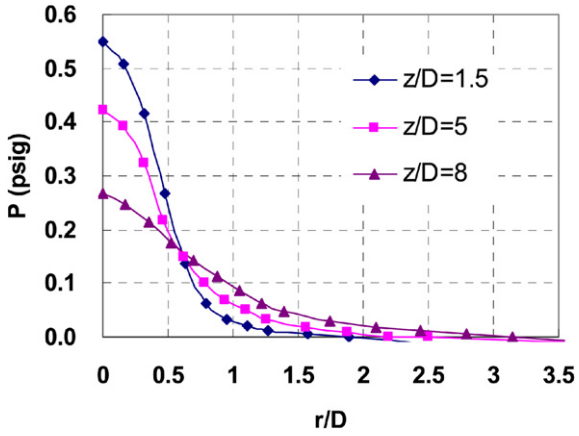

Fig. 7. Distribution of static pressure over the impacted surface. $Re = 60\,000$.

Radial distribution of local Nu for $Z/D = 1.5$ and 5 are plotted in Fig. 11. Instead of having the highest heat transfer rate occurred at the stagnation point for all the other Z/D cases, the peak Nusselt number is found at about $r/D = 1.8$ when Z/D equals 1.5. This "second peak" locates right after the negative pressure gradient ends, according to the PSP result shown in Fig. 7. Therefore this local high heat transfer rate can be explained by the transition from laminar to turbulent boundary layer, which is triggered by the disappearance of the pressure gradient along the impinged surface. The second peak in Nu becomes less and less significant as Re decreases. When $Re = 10\,000$, there is merely a hump remains at the location of the second peak, the value of which is already lower than the stagnation point Nusselt number. For all the other Z/D cases, the Nusselt number decreases monotonically from the stagnation point. The disappearance of the "second peak" in Nu could be explained by the fact that the approaching velocity continuously decreases as a result of increasing Z/D, which leads to weaker flow acceleration at stagnation region compared to lower Z/D condition. The smaller pressure gradient near the stagnation zone diminishes the effect of transition from laminar to turbulent boundary layer. The non-zero slope at $r/D = 0$ is due to imperfection of curve-fit of the experimental data close to the stagnation point.

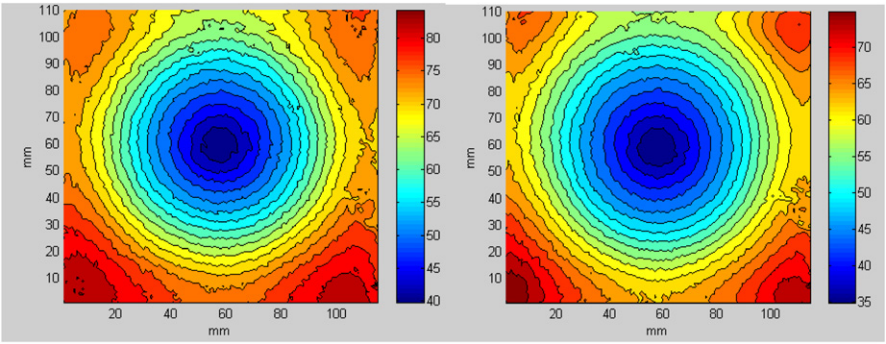

Left: Re=10000; Right: Re=60000

Z/D=5

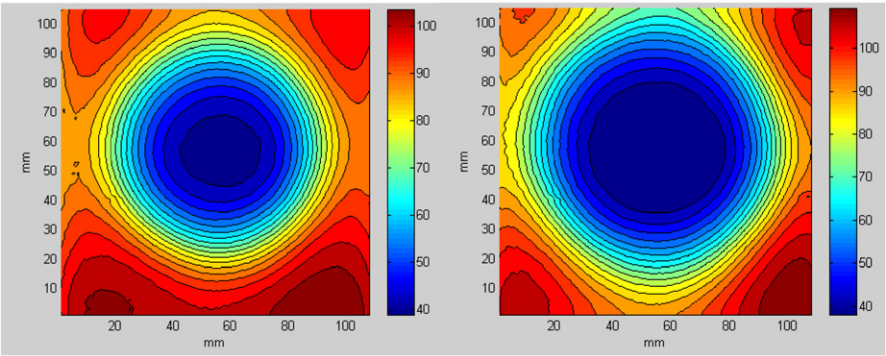

Left: *Re*=10000; Right: *Re*=60000

Z/D=1.5

Fig. 8. TSP temperature contours in °C.

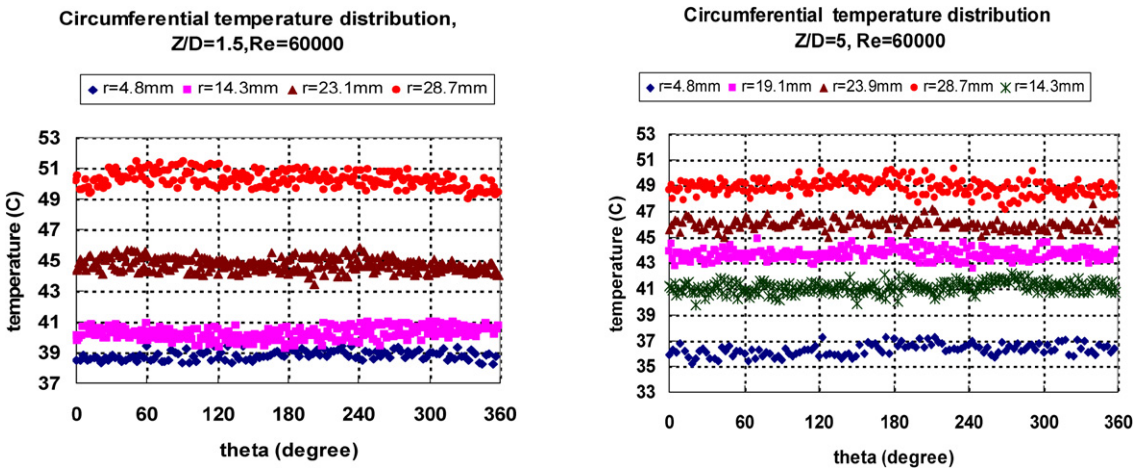

Fig. 9. Typical temperature variation in circumferential direction measured by TSP.

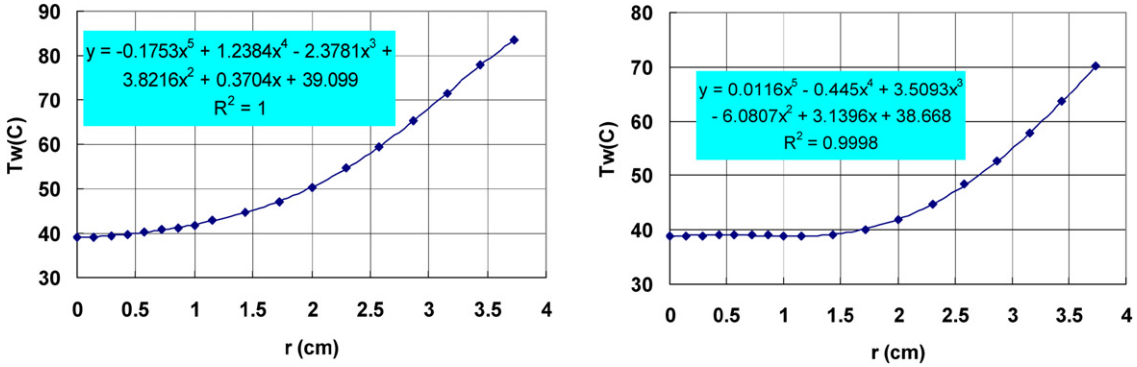

Fig. 10. Typical temperature plot as a function of r, $Z/D = 1.5$. Left: $Re = 10\,000$; Right: $Re = 60\,000$.

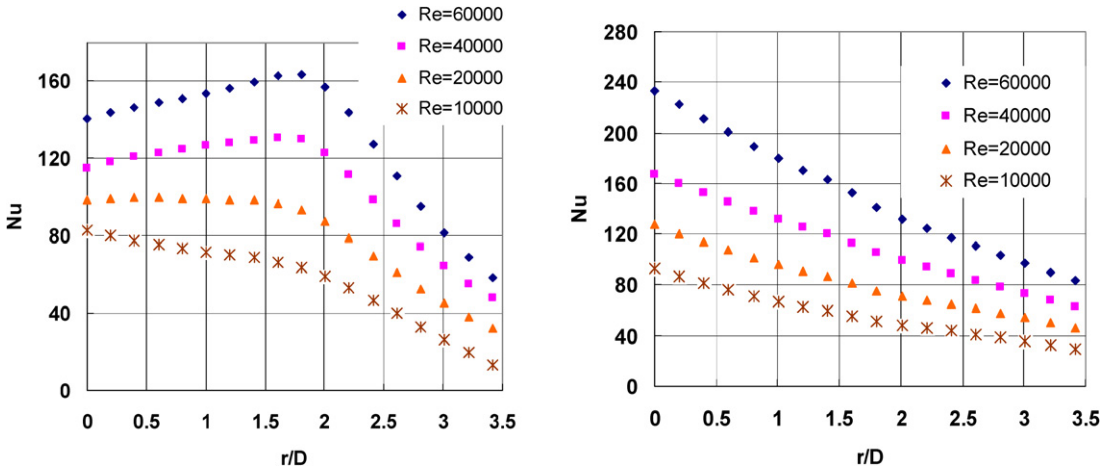

Fig. 11. Local Nu distribution for $Z/D = 1.5$ (left) and 5 (right).

Fig. 12 shows experimental and CFD local Nu for $Re = 60\,000$, $40\,000$ and $20\,000$ at $Z/D = 1.5$. The maximum difference between experimental and CFD Nu is found to be within 20% before the second peak in Nu occurs. Depart from the stagnation region, where $r/D > 2$, the experimental Nu decreases faster than the CFD prediction as r/D increases. Fig. 13 shows CFD path lines for $Z/D = 1.5$ and $Re = 60\,000$. The second peak location and its mechanism of occurrence are identified. The air after impinging on the stagnation zone starts to accelerate towards exits. At low Z/D of 1.5 a relatively large vortex is formed centered at r/D of approximately 2.5. Air is forced to impinge back again while it is continuously moving within this large vortex forming the second peak region.

The effect of Z/D on the stagnation point Nu_o is plotted in Fig. 14. Nu_o reaches maximum at about Z/D equal to 5. From the Pitot probe measurement it is found that the length of potential core is about 4 times the jet nozzle diameter. Beyond the potential core, with further increase in axial distance, the

interaction between the attenuation of approaching jet velocity and the continuous increase in centerline turbulence intensity brings about a maximum heat transfer coefficient at $Z/D \sim 5$.

Experimental results for average *Nu* are compared to those calculated using correlation for single jet from [4]:

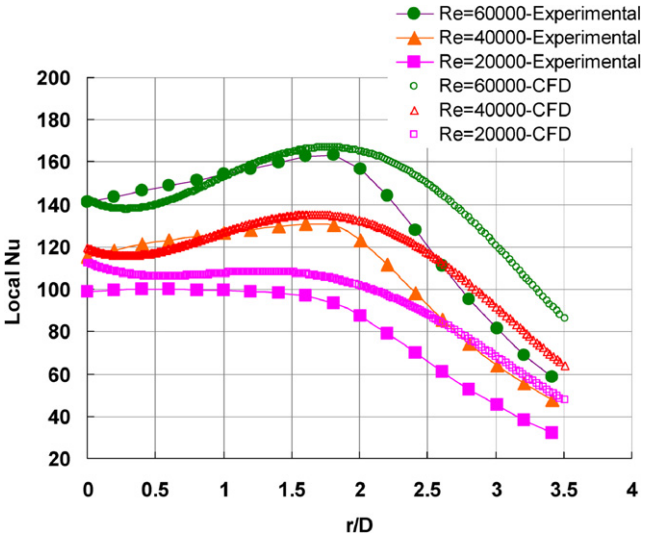

Fig. 12. Experimental and CFD *Nu*.

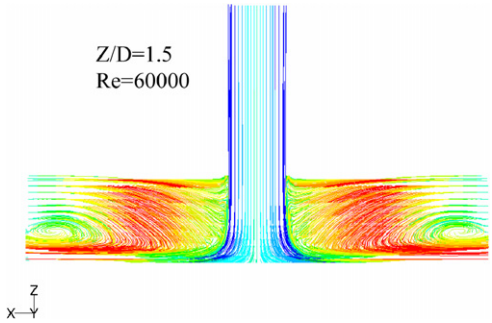

Fig. 13. CFD path lines colored by particle I.D.

$$\left(\frac{\overline{Sh}}{Sc^{0.42}}\right) = \left(\frac{\overline{Nu}}{Pr^{0.42}}\right) = \frac{D}{r}\frac{1-1.1D/r}{1+0.1(Z/D-6)D/r}F(Re)$$

$$\text{where } F(Re) = 2Re^{0.5}\left(1+\frac{Re^{0.55}}{200}\right)^{0.5} \tag{10}$$

The objective of comparison is to verify experimentally the validity of the correlation for low Z/D (<2) and low r/D (<2.5). The range of validity of Martin's correlation is: $2000 \leqslant Re \leqslant$

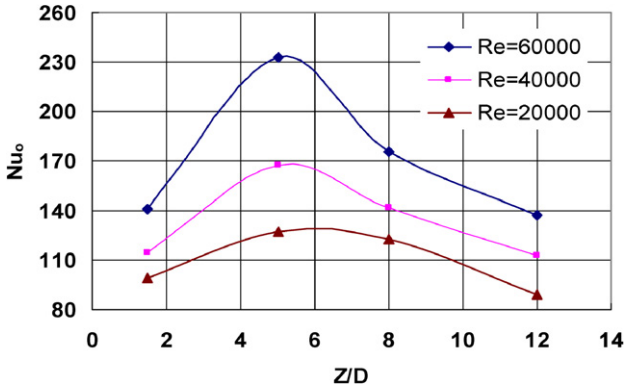

Fig. 14. Effect of Z/D on stagnation point Nu_o.

Table 1
Summary of average *Nu* benchmark comparison with correlation from Martin [4]

Re	Z/D	Difference $r/D = 2.5$ [%]	Difference $r/D = 3.5$ [%]
10 000	5	6.8	0.6
20 000	5	−1.5	−4.2
40 000	5	−9.8	−14.8
60 000	5	−10.6	−15.4
10 000	1.5	2.5	−10.2
20 000	1.5	−6.2	−13.3
40 000	1.5	−20.8	−24.7
60 000	1.5	−25.1	−28.2

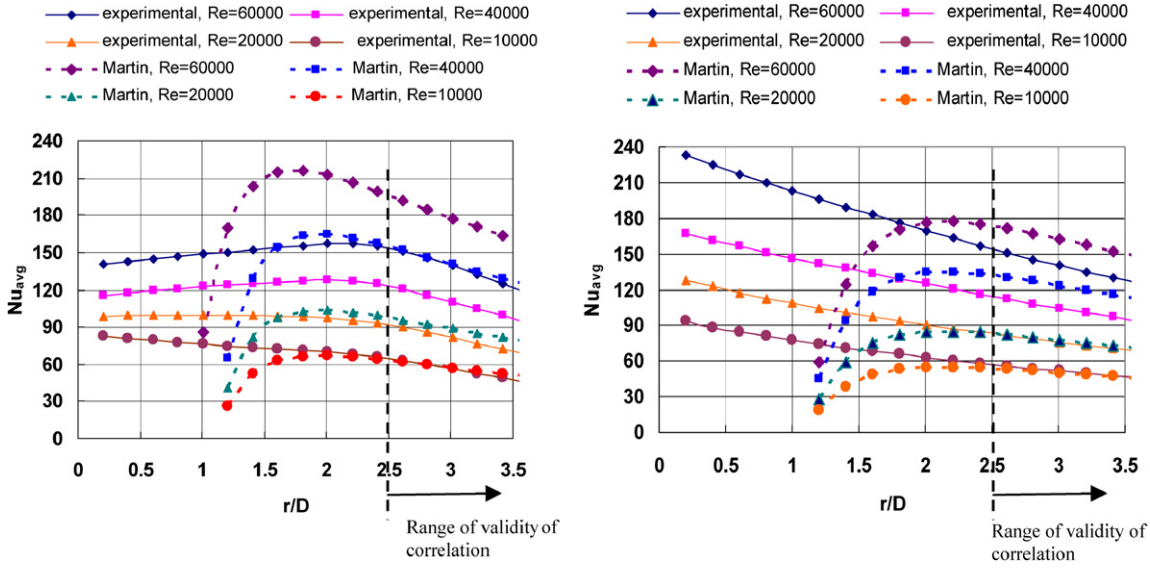

Fig. 15. Average *Nu* compared to Martin's correlation. Left: $Z/D = 1.5$; Right: $Z/D = 5$.

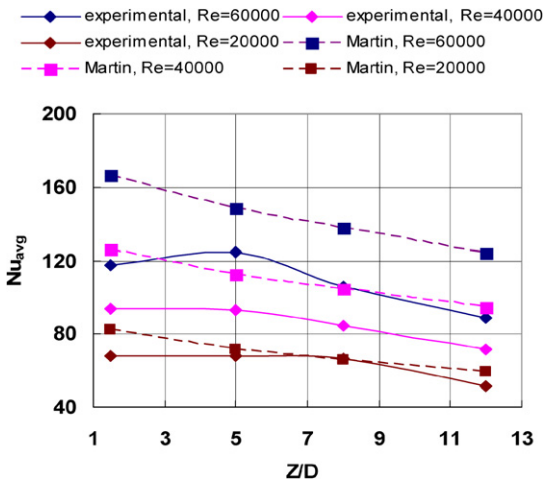

Fig. 16. Area averaged Nu (averaged over $r/D = 3.5$), compared with empirical data from Martin's (1977) correlation.

400 000; $2.5 \leqslant r/D \leqslant 7.5$; $2 \leqslant Z/D \leqslant 12$. The comparison is shown in Figs. 15 for Z/D of 5 and 1.5. The difference between experimental and empirical data are listed in Table 1 for $r/D = 2.5$ and 3.5. The difference in % is defined as: $100 * (\text{experimental} - \text{correlation})/\text{correlation}$.

Comparing experimental results of average Nu to those calculated using correlation for $Z/D = 1.5$ and 5, it is observed in Fig. 15 that: (1) As r/D increases, the empirical data decreases monotonically from the beginning of the valid range ($r/D = 2.5$); (2) The agreement is good for low Reynolds number of 10 000 and 20 000. Correlation overestimates Nu at all Z/D for higher jet Reynolds number of 40 000 and 60 000. The difference increases with jet Reynolds number as well as r/D, the latter indicates that the experimental Nusselt number decreases faster than the empirical one.

The area averaged Nusselt number Nu_{avg} is plotted in Fig. 16 against Z/D and also compared with Martin's empirical data. For $Z/D = 1.5$ and 5, the experimental values of Nu_{avg} are essentially the same for lower jet Reynolds number. At the highest Reynolds number of 60 000, the maximum Nu_{avg} appears at $Z/D = 5$. As Z/D further increases, the Nu_{avg} starts to decreases. Heat transfer data calculated from Martin's correlation are higher than the experimental data and the difference between them increases with increasing jet Reynolds number. Additionally, since empirical data decreases with Z/D monotonically, it could not reflect any possible optimum Z/D where Nusselt number reaches maximum. Comparatively, experimental average Nusselt number still has an optimum value at Z/D about 5, although this optimum is not as appreciable as stagnation point Nusselt number.

Conclusions

Experimental and computational studies are performed to study pressure, temperature distributions and flow patterns on impingement target surface subject to a single impinging air jet issuing from plenum. The following is concluded:

(i) The experimental results obtained by TSP and PSP measurement technique show similar trend compared to literature. The existence of an "optimal Z/D" and a "second peak" in local Nu other than stagnation point peak are both observed.
The optimal jet-to-target surface distance (Z/D) for area-averaged Nu is found to be about 5. The second peak in local Nu appears with Z/D of 1.5 and r/D of 1.8. The disappearance of the "second peak" in local Nu as Z/D increases beyond the potential core might be explained by the reduced pressure gradient near the stagnation zone.

(ii) For $Z/D = 1.5$, CFD simulation captures reasonably well the shape of Nusselt number profile up to $r/D = 3.5$.

(iii) Experimental average Nu are compared to that calculated using correlation from Ref. [4]. The difference varies with Z/D and jet Reynolds number. The disagreement might result from the difference in the jet nozzle configuration since the reference correlation is based on the experimental data that obtained with either a long tube-type nozzle or a shaped nozzle with a smooth contraction.

References

[1] R.J. Goldstein, A.I. Behbahani, Impingement of a circular jet with and without cross flow, International Journal of Heat and Mass Transfer 25 (1982) 1377.
[2] R.J. Goldstein, J.F. Timmers, Visualization of heat transfer from arrays of impinging jets, International Journal of Heat and Mass Transfer 25 (1982) 1857.
[3] E.M. Sparrow, R.J. Goldstein, Effects of nozzle-surface separation distance on impingement heat transfer for a jet in a crossflow, ASME Journal of Heat Transfer (1975) 528–533.
[4] H. Martin, Impinging jet flow heat and mass transfer, Advances in Heat Transfer 13 (1977) 1–61.
[5] J.-C. Han, S. Dutta, S.V. Ekkad, Gas turbine heat transfer and cooling technology, 2000.
[6] S.J. Downs, E.H. James, Jet impingement heat transfer—A literature survey, Presented at National Heat Transfer Conference, Pittsburgh, PA, 1987.
[7] R. Viskanta, Heat transfer to impinging isothermal gas and flame jets, Experimental Thermal and Fluid Science 6 (1993) 111–134.
[8] J.N.B. Livingood, P. Hrycak, Impingement heat transfer from turbulent air jets to flat plates—a literature survey, NASA TR I-2778, 1973.
[9] R. Gardon, J. Cobonpue, Heat transfer between a flat plate and jets of air impinging on it, International Developments in Heat Transfer, ASME (1963) 454–460.
[10] R.J. Goldstein, A.I. Behbahani, K. Heppelmann, Streamwise distribution of the recovery factor and the local heat transfer coefficient to an impinging circular air jet, International Journal of Heat and Mass Transfer 29 (1986) 1227.
[11] R. Gardon, J.C. Akfirat, The role of turbulence in determining the heat transfer characteristics of impinging jets, International Journal of Heat and Mass Transfer 8 (1965) 1261–1272.
[12] C. Donaldson, R. Snedeker, D.P. Margolis, A study of free jet impingement. Part 2. Free jet turbulent structure and impingement heat transfer, Journal of Fluid Mechanics 45 (1971) 477–512.
[13] C.O. Popiel, O. Trass, Visualization of free and impinging round jets, Experimental Thermal and Fluid Science 4 (1991) 253.
[14] V. Narayanan, J. Seyed-Yagoobi, R.H. Page, An experimental study of fluid mechanics and heat transfer in an impinging slot jet flow, International Journal of Heat and Mass Transfer 47 (2004) 1827–1845.
[15] J.-Y. San, W.-Z. Shiao, Effects of jet plate size and plate spacing on the stagnation Nusselt number for a confined circular air jet impinging on a flat surface, International Journal of Heat and Mass Transfer 49 (2006) 3477–3486.